

Improving the Plausibility of Pressure Distributions Synthesized from Depth Image through Generative Modeling

Neevkumar Manavar¹ Hanno Gerd Meyer¹ Joachim Waßmuth¹
Barbara Hammer² Axel Schneider¹

¹Hochschule Bielefeld, Interaktion 1, Bielefeld, Germany

²CITEC, Bielefeld University, Inspiration 1, Bielefeld, Germany

{neevkumar.manavar, hanno-gerd.meyer, joachim.waßmuth, axel.schneider}@hsbi.de

bhammer@techfak.uni-bielefeld.de

Abstract

Monitoring contact pressure in hospital beds is essential for preventing pressure ulcers and enabling real-time patient assessment. Current methods can predict pressure maps but often lack physical plausibility, limiting clinical reliability. This work proposes a framework that enhances plausibility via Informed Latent Space (ILS) and Weight Optimization Loss (WOL) with conditional generative modeling to produce high-fidelity, physically consistent pressure estimates. This study also applies diffusion based conditional Brownian Bridge Diffusion Model (BBDM) and proposes training strategy for its latent counterpart Latent Brownian Bridge Diffusion Model (LBBDM) tailored for pressure synthesis in lying postures. Experiment results shows proposed method improves physical plausibility and performance over baselines: BBDM with ILS delivers highly detailed maps at higher computational cost and large inference time, whereas LBBDM provides faster inference with competitive performance. Overall, the approach supports non-invasive, vision-based, real-time patient monitoring in clinical environments.

1. Introduction

The global prevalence of hospitalized adult patients with pressure injuries is 12.8%, with an incidence rate of 5.4 per 10,000 patient days [24]. Mechanical factors such as shear force, friction, and pressure remain the leading risk contributors [12]. Several wearable medical devices have been proposed to monitor patients’ risk of pressure ulcer development [22, 35]; however, these devices often contribute to pressure-related injuries [4, 18, 20].

To prevent pressure injuries caused by mechanical boundary conditions, repositioning patients every two hours

is a commonly used practice [11]. However, continuous contact pressure monitoring of lying patients is critical for understanding, prevention, and timely intervention against pressure injuries [14, 31]. Beyond traditional active pressure monitoring systems [3, 34], recent studies have explored predicting contact pressure distributions using non-invasive, vision-based approaches. For instance, [Clever et al. \[8\]](#) and [Manavar et al. \[28\]](#) predict 2D pressure distributions of individuals lying in bed using depth images.

The method by [Clever et al. \[8\]](#) employs a deep neural network encoder followed by a white-box reconstruction model for pressure estimation. In contrast, [Manavar et al. \[28\]](#) introduced the Attention Feature Network (ATTNFNET) with a Conditional Generative Adversarial Network (CGAN) framework to synthesize pressure distributions. While these approaches outperform baselines, problem of physically implausible distributions persist [28].

To address this issue, we propose an improved framework for generating plausible pressure distributions. The study introduces the Informed Latent Space (ILS) and Weight Optimization Loss (WOL) modules, to tackle this problem. We build upon the AttnFNet architecture as the base model, which encodes depth images into a latent space, while anthropometric factors such as mass, height, and gender are conditioned through cross-attention within this space. During training, the encoded mass information is further optimized using WOL.

A major limitation of prior methods is their weak modeling of how pressure depends on human attributes (mass, height, gender). The proposed ILS addresses this by explicitly coupling these factors, producing more plausible and adaptive pressure maps. A practical advantage is the model’s body parameter adaptation: for the same subject’s depth image, adjusting mass, height, or gender yields distinct, physically consistent pressure distributions. This

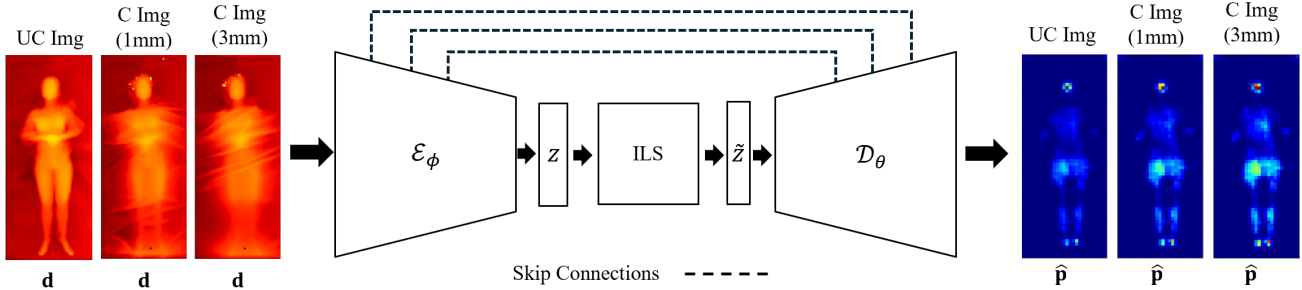


Figure 1. Overview of the model architecture with the integration of the ILS module. The model takes a single depth image as input and generates the pressure distribution.

adaptability is clinically useful when patient characteristics change over time, since only the conditioning inputs need updating rather than retraining the model.

This study also introduces pressure synthesis via a conditional Brownian Bridge Diffusion Model (BBDM) and Latent Brownian Bridge Diffusion Model (LBBDM) [23]. We employed a two-stage training strategy for a conditional LBBDM, tailored for pressure synthesis. Additionally, a VQGAN model [42] trained on a distinct objective is integrated with the LBBDM for pressure generation. To see the impact of ILS in the diffusion process, we have incorporated ILS into the denoising model and into the pretrained ATTNFNET network when using conditional LBBDM.

We evaluate the proposed method on the publicly available Systematic Lying Postures (SLP) dataset [27] and compare it against established baselines [8, 28].

2. Related Work

Pressure Injury Prevention: According to the European Pressure Ulcer Advisory Panel (EPUAP) [12], mechanical boundary conditions are one of the causes of pressure ulcer development. Injury formation occurs due to boundary conditions such as the magnitude, duration, and time of the applied mechanical load. Patients with mobility impairments are particularly vulnerable to such conditions.

Conventionally, nurses reposition bedridden patients every two hours to reduce skin hydration, minimize prolonged mechanical load, and redistribute pressure [29]. As this repositioning frequency dates back to World War II [11], it remains a standard method for preventing pressure injuries caused by mechanical boundary conditions. However, studies by Peterson et al. [32, 33] suggest that the current repositioning protocol requires improvement, as poor pressure redistribution can still occur despite the scheduled turning.

In light of this, inferring accurate pressure distributions for a lying person is essential to understanding ulcer formation caused by mechanical factors and enabling timely intervention [14, 31]. Building upon this concept, this paper addresses the problem through a non-invasive, lightweight,

vision-based system that infers biomechanical contact pressure distributions from a single depth camera.

Patient Monitoring Systems and Pressure Synthesis:

The most common approach for monitoring biomechanical contact pressure is through direct sensing devices [3, 34], which have been improved by techniques such as body part localization [25] and automatic limb identification [2] to aid pressure injury prevention.

Several studies have focused on classifying the postures of lying humans [9, 19, 38]. Later, Liu et al. [27] introduced the SLP dataset, enabling in-bed human pose monitoring [1, 7, 10, 30, 36, 41].

Alternatively, some researchers proposed vision-based pressure estimation approaches. Grady et al. [15] proposed an RGB camera-based pressure estimation method, while Liu and Ostadabbas [26] developed the Pressure Eye (PEYE) network, which infers pressure images from RGB inputs using a pixel-wise resampling approach. Further advancements were made by Clever et al. [8] and Manavar et al. [28], who predicted pressure distributions from single depth images.

Clever et al. [8] proposed BPBnet and BPWnet to infer contact pressure distributions using a network that embeds a human body mesh model and employs a white-box model for pressure reconstruction. Later, Manavar et al. [28] introduced the ATTNFNET model, which incorporates mixed-domain loss and a CGAN training strategy for pressure inference using the SLP dataset.

Building on these prior concepts, the proposed study introduces a novel approach for inferring plausible pressure distributions through conditional generative modeling. This study proposes the inclusion of anthropometric information to build interdependencies via ILS, and further improving pressure plausibility through WOL when predicting distributions in pixel space. Furthermore, in our work, we synthesized pressure distributions using conditional BBDM, evaluated the impact of ILS during diffusion denoising BBDM + ILS, and introduced a two-stage training approach for a conditional LBBDM tailored for pres-

sure synthesis. To the authors’ knowledge, no prior work has applied diffusion-based modeling for predicting pressure distributions.

Optimization for Plausibility: Although previous methods successfully infer pressure from single depth images, the synthesized pressure distributions often lack physical plausibility, even when achieving low metric scores in Mean Squared Error (MSE) and Structural Similarity Index (SSIM) [28]. While BPWnet and ATTNFNET outperform earlier baselines in MSE, they still fail to produce distributions that align with actual weight measurements [8, 28]. Relying on auxiliary networks like Betanet [8] is insufficient, as it only estimates body parameters rather than enforcing physical plausibility directly within the pressure generation pipeline.

Although Betanet predicts height and mass, this component remains independent of BPBnet and BPWnet, and does not establish any interrelationships between pressure and anthropometric attributes. Similarly, the approach proposed by Manavar et al. [28] lacks a mechanism to model such dependencies.

This study addresses these challenges by proposing an informed mechanism to incorporate plausibility into pressure inference through ILS and WOL. Additionally, ILS is integrated into the denoising process of the BBDM during training and into the pretrained network during LBBDM training to investigate its influence on pressure plausibility in diffusion denoising.

3. Methods

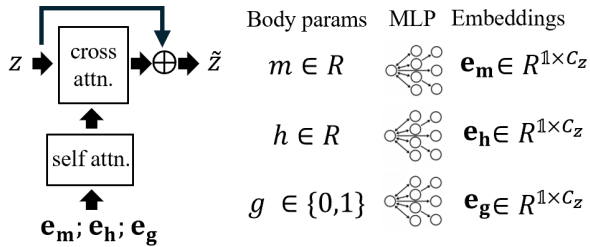


Figure 2. Overview of the ILS module, consisting of anthropometric embedding self-attention and image-embedding cross-attention to generate the informed latent \tilde{z} from latent z .

The method section describes the inclusion of ILS, WOL, and pressure synthesis using conditional BBDM and LBBDM [23].

3.1. Drawing Meaningful Samples through ILS

Let $\mathbf{d} \in \mathbb{R}^{H_d \times W_d}$ represent the input depth image and $\mathbf{p} \in \mathbb{R}^{H_p \times W_p}$ represent the pressure image, where H_d and W_d

denote the height and width of the depth image, and H_p and W_p denote the height and width of the pressure image.

$$z = \mathcal{E}_\phi(\mathbf{d}) \quad (1)$$

The depth image is encoded using $\mathcal{E}_\phi(\mathbf{d})$, parameterized by ϕ . It produces a latent feature map $z \in \mathbb{R}^{C_z \times H_z \times W_z}$ for one sample, as shown in Eq. (1), where C_z represents the latent embedding dimension.

$$\hat{\mathbf{p}} = \mathcal{D}_\theta(z; \{\mathbf{s}_1, \mathbf{s}_2, \dots, \mathbf{s}_L\}) \quad (2)$$

The decoder $\mathcal{D}_\theta(z; \{\mathbf{s}_1, \mathbf{s}_2, \dots, \mathbf{s}_L\})$ takes the latent feature map along with optional skip connections and produces the pressure image $\hat{\mathbf{p}}$.

The latent feature map z produced by the encoder has no Body-Mass (BM), body-height, or gender awareness during training if the model is trained without incorporating additional information into the model architecture. To encode anthropometric information into the model, we condition this information in the latent space.

Let the anthropometric information include BM $m \in \mathbb{R}$, height $h \in \mathbb{R}$, and gender $g \in \{0, 1\}$. These parameters pass through a learnable linear layer to generate encodings, as shown in Eq. (3). Before passing the BM m and body-height h values to the MLP layer, we normalize them by dividing by the largest possible values of BM and body-height in the dataset.

$$\begin{aligned} e_m &= \text{MLP}_m(m; \theta_m) \in \mathbb{R}^{1 \times C_z} \\ e_h &= \text{MLP}_h(h; \theta_h) \in \mathbb{R}^{1 \times C_z} \\ e_g &= \text{MLP}_g(g; \theta_g) \in \mathbb{R}^{1 \times C_z} \end{aligned} \quad (3)$$

The individual parameter embeddings are aggregated into a unified conditioning representation resulting in a sequence of three conditioning tokens Eq. (4), where $[\cdot; \cdot]$ denotes concatenation.

$$\mathbf{E}_{m,h,g} = [e_m; e_h; e_g] \in \mathbb{R}^{3 \times C_z} \quad (4)$$

Concatenated encodings then pass through standard multi-headed self-attention layer to model inter-parameter relationships, as shown in Eq. (5) [39].

$$\text{Attn}_{m,h,g} = \text{layernorm}(\text{MHA}(E_{m,h,g}, E_{m,h,g}, E_{m,h,g})) \quad (5)$$

To condition the anthropometric attention output Eq. (5), the latent representation z is first flattened along the sequence dimensions and transposed for cross-attention conditioning: $z \in \mathbb{R}^{d_z \times C_z}$, where d_z denotes the sequence length ($H_z \times W_z$).

Finally, to integrate anthropometric information into the latent space, the attention output of the anthropometric information $\text{Attn}_{m,h,g}$ Eq. (5) is used as the key in a multi-

headed cross-attention operation on the latent representation z , as illustrated in Eq. (6).

$$\tilde{z} = \text{layernorm}(z + \text{MHA}(z, \text{Attn}_{m,h,g}, \text{Attn}_{m,h,g})) \quad (6)$$

Instead of drawing samples from the latent representation z , the decoder now draws more meaningful samples from the informed latent $\tilde{z} \in \mathbb{R}^{C_z \times H_z \times W_z}$, improving the plausibility of the generated pressure distributions Eq. (7).

$$\tilde{\mathbf{p}} = \mathcal{D}_\theta(\tilde{z}; \{\mathbf{s}_1, \mathbf{s}_2, \dots, \mathbf{s}_L\}) \quad (7)$$

3.2. Reducing Total Body-Mass Error through WOL

The recorded actual pressures are obtained from the pressure mat positioned beneath the subjects [27]. For bodies at rest, the force acting upon the pressure mat corresponds to the gravitational force (Mg), where M denotes the BM of the person lying on the bed, and g represents the gravitational acceleration.

The pressure acting on the i^{th} sensor is defined by Eq. (8).

$$p_i = \frac{M_i g}{A_i} \quad (8)$$

The total BM of the person can be estimated from the pressure distribution using Eq. (9) [28], where N is the total number of sensors and A_i denotes the area of the i^{th} sensor.

$$M = \sum_{i=1}^N \frac{p_i A_i}{g} \quad (9)$$

The predicted BM \hat{M} is computed from the predicted pressure distribution \hat{p} using Eq. (9). To minimize the body-mass estimation error, the mean absolute difference between the predicted BM \hat{M} and the calculated BM M is used. From Eq. (9) we can derive WOL as Eq. (10) (more in supplementary material Sec. 7), which reduces the total BM error and improves the plausibility of the pressure distributions inferred from the depth image.

$$\mathcal{L}_{WOL} = \left| \sum_{i=1}^N (p_i - \hat{p}_i) \right| \quad (10)$$

3.3. Training Strategy

This study employs conditional generative modeling approaches such as cGAN, BBDM, and LBBDM to synthesize pressure distributions.

We have used the encoder-decoder model architecture introduced by Manavar et al. [28] when predicting pixels. For diffusion model training, we use OpenAI’s improved

U-Net as the denoising model, consistent with the setup by Li et al. [23].

As our first use case, the ATTNFNET model is trained with a combination of adversarial loss, perceptual loss, pixel loss, and weight optimization loss (WOL). The model is trained with the objectives shown in Eq. (11), Eq. (12), additionally incorporating the ILS.

$$\begin{aligned} \mathcal{L}_D = & - \left[\mathbb{E}_{\mathbf{d}, \mathbf{p}} [y_{\text{real}} \cdot \log(D(\mathbf{d}|\mathbf{p}))] \right. \\ & + \mathbb{E}_{\mathbf{d}, \mathbf{p}} [(1 - y_{\text{real}}) \cdot \log(1 - D(\mathbf{d}|\mathbf{p}))] \\ & + \mathbb{E}_{\mathbf{d}} [y_{\text{gen}} \cdot \log(D(\mathbf{d}|G(\mathbf{d})))] \\ & \left. + \mathbb{E}_{\mathbf{d}} [(1 - y_{\text{gen}}) \cdot \log(1 - D(\mathbf{d}|G(\mathbf{d})))] \right] \quad (11) \end{aligned}$$

$$\begin{aligned} \mathcal{L}_G = & \left[- \mathbb{E}_{\mathbf{d}} [\log(D(\mathbf{d}|G(\mathbf{d})))] \right. \\ & \left. + \lambda \cdot \mathbb{E}_{\mathbf{d}, \mathbf{p}} [\alpha \mathcal{L}_{SSIM} + \beta \mathcal{L}_{L2} + \gamma \mathcal{L}_{WOL}] \right] \quad (12) \end{aligned}$$

The discriminator is a PatchGAN like [17]. Label values for y_{gen} and y_{real} are set to 0.1 and 0.9, respectively. The loss weight for λ is set to 100, and the ratio of α , β , and γ is 3 : 0.01 : 0.01. Here, \mathcal{L}_{SSIM} is the SSIM loss, and \mathcal{L}_{L2} is the MSE loss [28].

For the BBDM training, we follow the procedure described by Li et al. [23] using OpenAI’s U-Net model. However, the condition \mathbf{y} is concatenated with the diffused image \mathbf{x}_t as input to the model, enabling it to retain the conditioning information. The following objective is used during training Eq. (13).

$$\mathbb{E}_{\mathbf{x}_0, \mathbf{y}, \epsilon} [\| m_t(\mathbf{y} - \mathbf{x}_0) + \sqrt{\delta_t} \epsilon - \epsilon_\theta(\mathbf{x}_t | \mathbf{y}, t) \|^2] \quad (13)$$

Here, \mathbf{y} is the conditioning input (depth image \mathbf{d}), \mathbf{x}_0 is the clean target image (pressure image \mathbf{p}), and $\epsilon \in \mathcal{N}(0, I)$ represents Gaussian noise. The variable \mathbf{x}_t denotes the diffused data (diffused pressure image) at time step t , ϵ_θ is the denoising function, and m_t is defined as $m_t = \frac{t}{T}$, where T denotes the total number of diffusion time steps. The term δ_t represents the variance.

The forward diffusion process is described in Eq. (14).

$$\mathbf{x}_t = (1 - m_t) \mathbf{x}_0 + m_t \mathbf{y} + \sqrt{\delta_t} \epsilon_t \quad (14)$$

To infer the pressure image \mathbf{p} from the depth image \mathbf{d} , we employ a non-Markovian process while preserving the original marginal distribution as in a Markovian inference process. We use a sequence length of $S = 200$ to accelerate the sampling process. For the diffusion steps $t = [0 : T]$, a marginally distributed subset is defined by $t_s = [0, \tau_1, \tau_2, \dots, \tau_s]$.

$$\begin{aligned}
\mathbf{x}_{t_s-1} &= (1 - m_{t_s-1}) \mathbf{x}_{\tilde{0}} + m_{t_s-1} \mathbf{y} \\
&+ \sqrt{\frac{\delta_{t_s-1} - \tilde{\delta}_{t_s}}{\delta_{t_s}}} (\mathbf{x}_{t_s} - (1 - m_{t_s}) \mathbf{x}_{\tilde{0}} - m_{t_s} \mathbf{y}) \\
&+ \sqrt{\tilde{\delta}_{t_s}} z
\end{aligned} \tag{15}$$

Sampling Algorithm

1. Sample conditional input $\mathbf{x}_T = \mathbf{y} \sim q(\mathbf{d})$
 2. **for** $t_s = \tau_s, \dots, \tau_1$ **do**
 3. $z \sim \mathcal{N}(0, \mathbf{I})$ if $t_s > 1$, else $z = 0$
 4. Sample \mathbf{x}_{t_s-1} Eq. (15)
 5. **return** \mathbf{x}_0
-

During the BBDM forward process, the data \mathbf{x}_0 gradually converges toward \mathbf{y} . By doing so, the model is encouraged to predict noise in a manner that reconstructs the original pressure distribution from the conditioning input \mathbf{y} (depth image) during inference. Algorithm 1 describes the sampling procedure of BBDM, where $\mathbf{x}_{\tilde{0}}$ is defined as $\mathbf{x}_{t_s} - \epsilon_{\theta}(\mathbf{x}_t | \mathbf{y}, t)$, and $\tilde{\delta}_{t_s}$ represents the posterior variance.

Because BBDM predicts noise, we cannot use WOL Eq. (10) since it is irrelevant to the main objective. However, we integrate ILS into OpenAi’s U-Net architecture to evaluate whether it can help the denoising process and produce more plausible results.

Finally, we employed BBDM in the latent space to evaluate computational performance improvements alongside the quality of generated pressure distributions. The ATTNFNET model was trained in a self-reconstruction manner using ILS to encode the relationships among mass, height, and gender during image reconstruction. Skip connections in the ATTNFNET architecture were removed to minimize the influence of the encoder during the decoding process. To reduce the size of the denoising model, a second bottleneck layer was introduced after the bottleneck layer to decrease the feature channel dimensionality (see supplementary Fig. 7).

The model was trained in an unconditional Generative Adversarial Network (GAN) setting with an unconditional PatchGAN discriminator and a modified ATTNFNET. The following objectives were used during pretraining Eq. (16) and Eq. (17), where \mathbf{x} denotes the model input and $\hat{\mathbf{x}}$ represents the reconstructed output generated by the autoencoder.

$$\begin{aligned}
\mathcal{L}_D &= -\mathbb{E}_{\mathbf{x}} \left[y_{\text{real}} \cdot \log(D(\mathbf{x})) \right. \\
&+ (1 - y_{\text{real}}) \cdot \log(1 - D(\mathbf{x})) \\
&+ y_{\text{gen}} \cdot \log(D(G(\mathbf{x}))) \\
&\left. + (1 - y_{\text{gen}}) \cdot \log(1 - D(G(\mathbf{x}))) \right]
\end{aligned} \tag{16}$$

$$\begin{aligned}
\mathcal{L}_G &= \left[-\mathbb{E}_{\mathbf{x}} [\log(D(G(\mathbf{x}))) \right] \\
&+ \lambda \cdot \mathbb{E}_{\mathbf{x}, \hat{\mathbf{x}}} [\alpha \mathcal{L}_{SSIM} + \beta \mathcal{L}_{L2}]
\end{aligned} \tag{17}$$

Post-training was performed using LBBDM in the latent space, following the objective described in Eq. (13). Samples were inferred from the latent space of the depth image using Algorithm 1 to obtain the pressure latent representation. The ATTNFNET decoder was subsequently used to generate pressure distributions from the denoised latent features.

This study also utilized an unconditionally trained VQ-GAN [42] model on the CelebHQ dataset [21], in a manner consistent with the BBDM paper [23] and compared results.

4. Evaluation

Table 1. Dataset splits and counts of uncovered (Ucov) and covered (cov) images, including 1 mm and 3 mm coverage variants.

Real + Synthetic Data (208K)				
Img Description	Ucov	cov (1mm)	cov (3mm)	total Img
real train (61)	2745	2745	2745	8235
real val (20)	900	900	900	2700
real test (20)	900	900	900	2700
total real	4500	4500	4500	13635
Synth Img	97495	97495		194990
Total training				203225
Total validation				2700
Total test				2700

4.1. Dataset

The Systematic Lying Postures (SLP) dataset [27] contains 102 healthy participants under three cover conditions and 45 unique poses, grouped into three sleeping postures (supine, left lateral, and right lateral). Cover conditions include uncovered poses, poses covered by a 1 mm blanket, and poses covered by a 3 mm blanket.

All experiments used both depth and pressure image modalities, with anthropometric information (BM, body-height, gender) integrated. Occlusion Free Depth Images (OFDI) data were used in place of raw depth images [5, 28]. Synthetic samples generated by Clever [6] augmented training data, including both uncovered and covered poses representing the real data blanket conditions [8].

Experiments followed a 60 : 20 : 20 split for training, validation, and testing. The splits were based on the 102 real participants, while synthetic data were added only to

Table 2. Test-set comparison of MPPA, MSSIM, MFID, MSE, and MPSNR across methods at three training sample sizes. ATTNFNET-143M and ATTNFNET-11M describes ATTNFNET model with 143 million and 11 million parameters respectively.

Method	Model	MPPA	MSSIM	MFID	MSE	MPSNR
3 k training samples						
Manavar et al. [28]	U-Net	0.6658	0.7958	0.4615	0.000433	34.4185
Manavar et al. [28]	ATTNFNET-143M	0.6142	0.8291	0.3475	0.000368	35.3508
Clever et al. [8]	BPBnet	0.0078	0.0204	160.58	0.00567	22.5927
Clever et al. [8]	BPWnet	0.5244	0.6331	1.6340	0.00405	24.1364
Ours	ATTNFNET-11M	0.6412	0.8864	1.0946	0.000263	36.2673
BBDM	Openai U-Net	0.0599	0.7783	0.1977	0.000197	37.3513
BBDM + ILS	Openai U-Net	0.5992	0.8730	0.6197	0.000346	34.9381
LBBDM VQGAN	pretrained VQGAN	0.0092	0.2611	1.5429	0.000777	31.2064
LBBDM	proposed pretraining	0.6950	0.8510	0.7338	0.000349	34.93
8 k training samples						
Manavar et al. [28]	ATTNFNET-11M	0.6793	0.8847	0.4323	0.000264	36.3225
Ours	ATTNFNET-11M	0.6451	0.8795	0.6979	0.000270	36.1675
BBDM	Openai U-Net	0.6772	0.9142	0.4381	0.000269	36.2827
BBDM + ILS	Openai U-Net	0.6679	0.9158	0.3465	0.000259	36.5109
LBBDM	proposed pretraining	0.7068	0.8507	0.9406	0.000313	35.4798
203 k training samples						
Manavar et al. [28]	ATTNFNET-11M	0.6580	0.8860	0.8014	0.000262	36.4592
Ours $\gamma = 0.0182$	ATTNFNET-11M	0.6539	0.8942	0.7993	0.000247	36.7770
BBDM	Openai U-Net	0.6306	0.8901	0.4267	0.000361	34.9244
BBDM + ILS	Openai U-Net	0.4146	0.8630	0.3821	0.000431	34.18

training. Subject 7 was excluded due to noise cleaning errors in the depth data [5]. Table 1 shows the detailed splits and image counts.

Real pressure images were pre-processed to reduce ambiguity, minimize data size, and align with prior studies. All real pressure images were resized to 27×64 and smoothed using a Gaussian filter ($\sigma = 1.4$) as in previous works [8, 28]. The original pressure range for synthetic data was (0, 101)kPa and for real data (0, 111)kPa; applying $\sigma = 1.4$ eliminated low-frequency high-pressure spikes and pressure in real data ranged between (0, 57)kPa.

Depth arrays were normalized individually to (0, 1) and pressure arrays were normalized globally by dividing by the maximum pressure value in the dataset.

4.2. Data Analysis

All models were evaluated under three different training conditions: (1) a sample size of 2745 (3k) using only uncovered postures from real data; (2) a sample size of 8235 (8k) including cover conditions from real data; and (3) a sample size of 203225 (203k) combining both real and synthetic data with all postures and covered conditions. All results are reported at epoch 100, unless stated otherwise.

Standard evaluation metrics for 2D images were used to

assess pressure generation quality: Mean Pixel Prediction Accuracy (MPPA) [28], Mean Structural Similarity Index (MSSIM) [40], Mean Fréchet Inception Distance (MFID) [37], MSE, and Mean Peak-Peak Signal-to-Noise Ratio (MPSNR) [13]. Fréchet inception distance (FID) was calculated with the original Inception-V3 model weights [16]. Table 2 presents metric scores for the proposed methods and baselines on the test dataset. In Tab. 2, BBDM with ILS outperformed all methods when trained on 8k samples, while our method with $\gamma = 0.0182$ outperformed in 203k training samples.

When images were rescaled from the normalized space, MSE was recalculated in pressure space as shown in Tab. 3. Consistent trends were observed: the proposed method displayed increased MSE in pressure space, but error rate declined when setting $\gamma = 0.0182$. Note that pressure ranges differ between real and synthetic data, and setting $\gamma = 1.0$ prevents the model from generating valid samples.

Participant BMs were calculated from actual and predicted pressure profiles using Eq. (9). Table 4 reports mean absolute BM differences among measured BMs (M_{meas}), BMs calculated from the ground truth pressures (M_{GT}), and from predicted pressures (M_{pred}). Further, BM plots in Fig. 3 enables detailed comparisons.

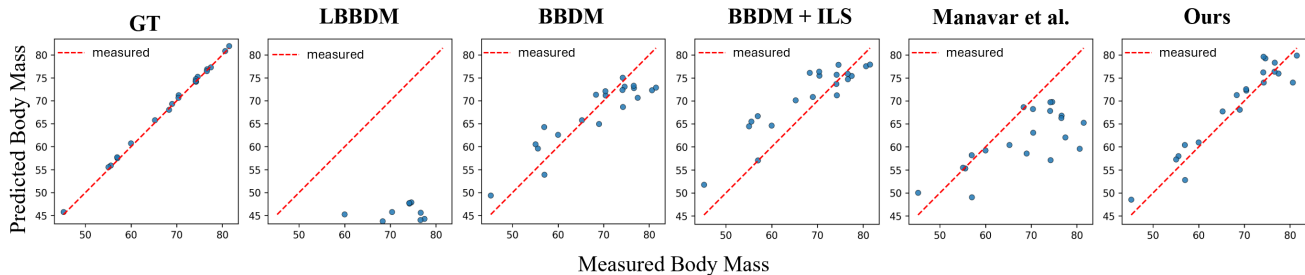


Figure 3. Scatter plot comparing BM computed from predicted pressure distributions across methods (blue points) with measured BM (red dotted identity line); GT denotes BM calculated from ground truth pressure distributions.

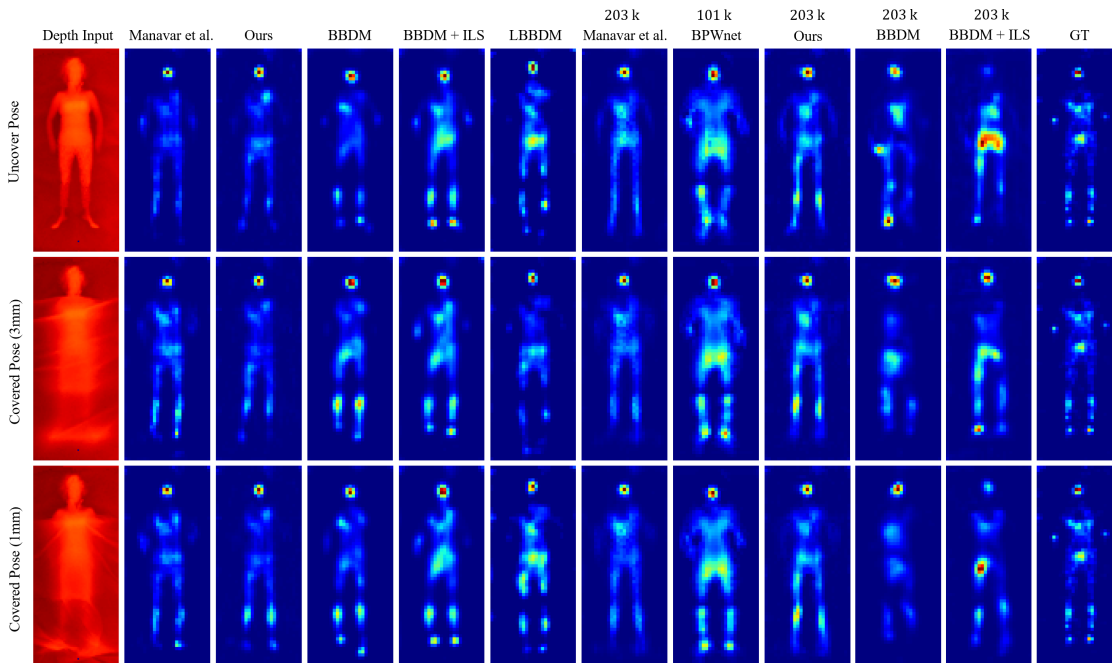


Figure 4. Qualitative comparisons of predicted pressure distributions against ground truths (GT) across representative samples; rows show different inputs to models and, each columns show model outputs.

Posture Intersection Over Union (IOU) [28] scores were computed to assess posture prediction error Tab. 5, and visual comparisons were used for qualitative analysis Fig. 4.

5. Ablation Study

An ablation study was conducted to assess the impact of ILS and WOL components on model performance and plausibility of generated results. Diffusion models were also evaluated with varying sampling steps to examine the effects on pressure generation quality.

Table 6 demonstrates that combining ILS and WOL yields more plausible pressure distributions with a slight increase in MSE. Table 7 presents the effect of the WOL

weight γ on MSE and BM Mean Absolute Error (MAE): reducing γ initially reduces the MSE but, increases the BM error.

For BBDM, increasing the number of sampling steps enhances diversity, as reflected by decreasing FID scores in Tab. 8, but also leads to higher MSE. The number of sampling steps does not directly affect BM estimation accuracy.

6. Discussion and Future Work

As shown in Tab. 7, decreasing γ reduces MSE but weakens BM-related information and thus plausibility. A value of $\gamma = 0.0182$ balances these objectives.

According to Tab. 2 and Tab. 3, BBDM+ILS and

Table 3. Test set MSE in kPa^2 for uncovered (Ucov), covered at 1 mm, covered at 3 mm, and overall poses, evaluated across methods at three training sizes.

Method	Ucov	cov (1mm)	cov (3mm)	overall
3 k training samples				
Manavar et al. [28]	0.6884	-	-	0.6884
Ours	0.7205	-	-	0.7205
BBDM	0.4817	-	-	0.4817
BBDM + ILS	0.8429	-	-	0.8429
LBBDM VQGAN	8.0909	-	-	8.0909
LBBDM	0.9580	-	-	0.9580
8 k training samples				
Manavar et al. [28]	0.7212	0.9134	0.9363	0.8570
BPWnet [8]	1.470	1.444	1.455	1.456
Ours	0.7567	0.9291	0.9442	0.8767
BBDM	0.5583	0.8146	0.8423	0.7384
BBDM + ILS	0.5141	0.7994	0.8224	0.7120
LBBDM	0.9047	1.0590	1.0803	1.0149
203 k training samples				
Manavar et al. [28]	0.7021	0.9224	0.9285	0.8510
BPBnet [8] 101K	0.772	0.858	0.884	0.838
BPWnet [8] 101K	1.155	1.190	1.209	1.184
Ours $\gamma = 0.0182$	0.6406	0.8814	0.8819	0.8013
BBDM	0.7990	1.077	1.0979	0.9914
BBDM + ILS	1.0031	1.2541	1.2926	1.1833

Table 4. Average Mean absolute body mass difference (kg) between measured and ground truth references versus predicted BMs, reported as $M_{\text{meas}} - M_{\text{pred}}$ and $M_{\text{GT}} - M_{\text{pred}}$; all models trained on 8 k real samples. best values are bolded

Method	Mean Absolute Body-Mass Difference (kg)	
	$M_{\text{meas}} - M_{\text{pred}}$	$M_{\text{GT}} - M_{\text{pred}}$
Manavar et al. [28]	7.28	7.50
ours	2.56	2.32
BBDM	3.88	3.75
BBDM + ILS	4.28	4.04
LBBDM	26.23	25.86
BPWnet (Betanet)	5.64	-

BBDM perform best when trained on real data only. However, performance degrades when trained on the larger 203 k dataset. We speculate that these models require more epochs to converge on the larger dataset compared to our method, though we could not validate this during training due to high inference times and limited compute resources. Nevertheless, Fig. 4 shows that BBDM+ILS produces vi-

Table 5. Posture Intersection over Union (IoU) on the 203 k training sample training, reported for uncovered (Ucov), covered at 1 mm, covered at 3 mm, and overall; best values are bolded.

Posture Intersection Over Union (203 k training samples)				
Method	Ucov	cov (1mm)	cov (3mm)	overall
Manavar et al. [28]	0.6561	0.6022	0.6010	0.6198
Ours $\gamma = 0.0182$	0.6675	0.6127	0.6096	0.6299
BBDM	0.6285	0.5605	0.5427	0.5772
BBDM + ILS	0.5102	0.4301	0.4214	0.4539

Table 6. Effect of the ILS and WOL components on prediction error: MSE of pressure maps and BM MAE. Model was trained using 8 k real samples.

Method	MSE (kPa^2)	BM MAE
ILS	0.8601	5.70
WOL	0.9151	5.53
ILS + WOL	0.8767	2.56

Table 7. Effect of the WOL weight γ on pressure MSE and BM MAE. Model was trained using 8 k real samples.

γ values	MSE (kPa^2)	BM MAE
$\gamma = 1.0$	0.8767	2.56
$\gamma = 0.1$	0.8760	2.63
$\gamma = 0.0182$	0.8903	2.74
$\gamma = 0.001$	0.8650	4.68

Table 8. Effect of diffusion sampling steps on pressure MSE, BM MAE, and FID; model was trained using 8 k real samples.

Sampling steps	MSE (kPa^2)	BM MAE	FID
$s = 10$	0.6797	4.02	0.4902
$s = 20$	0.6900	4.07	0.4833
$s = 100$	0.7273	3.86	0.4449
$s = 200$	0.7384	3.87	0.4381
$s = 500$	0.7500	3.90	0.4293
$s = 1000$	0.7521	3.88	0.4279

sually superior results compared to the standard BBDM.

A key requirement for using ILS in the model is establishing a prior global context for the features, as ILS cannot generate valid samples during training without it.

A current limitation is that plausibility is measured only via BM error. Future work should include region-specific metrics (e.g., errors at common pressure-injury sites) and additional plausibility criteria.

Another limitation is dataset composition: generation

quality reflects the mix of synthetic and limited real data. Future work will expand real datasets, diversify training, and assess cross-domain robustness. Further improvements require including patient data in training and conducting clinical validation, as current experiments involve healthy controls only.

While this study demonstrates promising capabilities for real-time monitoring (see supplementary Sec. 11), the system currently lacks a comprehensive quantitative assessment and large-scale validation in real-time settings.

Acknowledgments

This research was carried out within the framework of the project "SAIL: Sustainable Lifecycle of Intelligent Socio-Technical Systems". SAIL is receiving funding from the program "Netzwerke 2021", an initiative of the Ministry of Culture and Science of the State of North Rhine-Westphalia (grant No.: NW21-059B). The authors would like to acknowledge Dr. Matthias Fricke from the Center for Applied Data Science (CfADS) at Bielefeld University of Applied Sciences for providing access to the GPU compute cluster.

Conclusion

This work predicts physically plausible pressure distributions from a single depth image and explores conditional BBDM/LBBDM-based pressure synthesis. While BBDM with ILS yields the strongest metrics, the proposed approach with ILS and WOL achieves higher plausibility with faster training and inference with only a slight decrease in standard scores. Coupled with ATTNFNET, it points to a lightweight, non-invasive, real-time patient monitoring system.

References

- [1] Mohamed Afham, Udith Haputhanthri, Jathurshan Pradeepkumar, Mithunjha Anandakumar, Ashwin De Silva, and Chamira U. S. Edussooriya. Towards accurate cross-domain in-bed human pose estimation. In *ICASSP 2022 - 2022 IEEE International Conference on Acoustics, Speech and Signal Processing (ICASSP)*, pages 2664–2668, 2022. 2
- [2] Maziyar Baran Pouyan, Javad Birjandtalab, Mehrdad Nourani, and M.D. Matthew Pompeo. Automatic limb identification and sleeping parameters assessment for pressure ulcer prevention. *75(C):98–108*, 2016. 2
- [3] S. L. Bennett, R. Goubran, K. Rockwood, and F. Knoefel. Monitoring the relief of pressure points for pressure ulcer prevention: A subject dependent approach. In *2013 IEEE International Symposium on Medical Measurements and Applications (MeMeA)*, pages 135–138, 2013. 1, 2
- [4] Joyce M Black, Janet E Cuddigan, Maralyn A Walko, L Alan Didier, Maria J Lander, and Maureen R Kelp. Medical device related pressure ulcers in hospitalized patients. *International Wound Journal*, 7(5):358–365, 2010. 1
- [5] Henry Clever. SLP real cleaned up and reconstructed images, 2021. 5, 6
- [6] Henry Clever. BodyPressureSD, 2021. 5
- [7] Henry M. Clever, Zackory Erickson, Ariel Kapusta, Greg Turk, C. Karen Liu, and Charles C. Kemp. Bodies at Rest: 3D Human Pose and Shape Estimation From a Pressure Image Using Synthetic Data. In *2020 IEEE/CVF Conference on Computer Vision and Pattern Recognition (CVPR)*, pages 6214–6223, Los Alamitos, CA, USA, 2020. IEEE Computer Society. 2
- [8] Henry M. Clever, Patrick L. Grady, Greg Turk, and Charles C. Kemp. Bodypressure - inferring body pose and contact pressure from a depth image. *IEEE Transactions on Pattern Analysis and Machine Intelligence*, 45(1):137–153, 2023. 1, 2, 3, 5, 6, 8
- [9] William Cruz-Santos, Alberto Beltrán-Herrera, Eduardo Vázquez-Santacruz, and Mariano Gamboa-Zúñiga. Posture classification of lying down human bodies based on pressure sensors array. In *2014 International Joint Conference on Neural Networks (IJCNN)*, pages 533–537, 2014. 2
- [10] Thisun Dayarathna, Thamilu Muthukumarana, Yasiru Rathnayaka, Simon Denman, Chathura de Silva, Akila Pemasiri, and David Ahmedt-Aristizabal. Privacy-preserving in-bed pose monitoring: A fusion and reconstruction study. *Expert Systems with Applications*, 213:119139, 2023. 2
- [11] Tom Defloor, Katrien Vanderwee, Doris Wilborn, and Theo Dassen. *Pressure Ulcer Prevention and Repositioning*, pages 67–73. Springer London, London, 2006. 1, 2
- [12] European Pressure Ulcer Advisory Panel, National Pressure Injury Advisory Panel, and Pan Pacific Pressure Injury Alliance. *Prevention and Treatment of Pressure Ulcers/Injuries: Clinical Practice Guideline. The International Guideline*. EPUAP/NPIAP/PPPIA, 2019. 1, 2
- [13] Fernando A Fardo, Victor H Conforto, Francisco C De Oliveira, and Paulo S Rodrigues. A formal evaluation of psnr as quality measurement parameter for image segmentation algorithms. *arXiv preprint arXiv:1605.07116*, 2016. 6
- [14] Pallabi Ghosh, Prithevi Raj N, Vachana M N, Pavish S R, Prathibha Pereira, Tejeswini C J, Madhan Ramesh, Jehath Syed, and Sri Harsha Chalasani. Advances in technology-driven strategies for preventing and managing bedsores: A comprehensive review. *Archives of Gerontology and Geriatrics Plus*, 1(3):100029, 2024. 1, 2
- [15] Patrick Grady, Chengcheng Tang, Samarth Brahmabhatt, Christopher D. Twigg, Chengde Wan, James Hays, and Charles C. Kemp. Pressurevision: Estimating hand pressure from a single rgb image. In *Computer Vision – ECCV 2022*, pages 328–345, Cham, 2022. Springer Nature Switzerland. 2
- [16] Martin Heusel, Hubert Ramsauer, Thomas Unterthiner, Bernhard Nessler, and Sepp Hochreiter. Gans trained by a two time-scale update rule converge to a local nash equilibrium. In *Advances in Neural Information Processing Systems*. Curran Associates, Inc., 2017. 6
- [17] Phillip Isola, Jun-Yan Zhu, Tinghui Zhou, and Alexei A Efros. Image-to-image translation with conditional adversarial networks. In *CVPR*, 2017. 4

- [18] Debra Jackson, Ahmed M Sarki, Ria Betteridge, and Joanne Brooke. Medical device-related pressure ulcers: A systematic review and meta-analysis. *International Journal of Nursing Studies*, 92:109–120, 2019. 1
- [19] Chia-Feng Juang and Chia-Ming Chang. Human body posture classification by a neural fuzzy network and home care system application. *IEEE Transactions on Systems, Man, and Cybernetics - Part A: Systems and Humans*, 37(6):984–994, 2007. 2
- [20] Susan A. Kayser, Catherine A. VanGilder, Elizabeth A. Ayello, and Charlie Lachenbruch. Prevalence and analysis of medical device-related pressure injuries: Results from the international pressure ulcer prevalence survey. *Advances in Skin & Wound Care*, 31(6):276–285, 2018. 1
- [21] Cheng-Han Lee, Ziwei Liu, Lingyun Wu, and Ping Luo. Maskgan: Towards diverse and interactive facial image manipulation. In *Proceedings of the IEEE/CVF Conference on Computer Vision and Pattern Recognition (CVPR)*, 2020. 5
- [22] Soyeon Lee, Seung-Rok Kim, Kun-Hoo Jeon, Jun-Woo Jeon, Ey-In Lee, Jiwan Jeon, Je-Heon Oh, Ju-Hyun Yoo, Hye-Jun Kil, and Jin-Woo Park. A fabric-based wearable sensor for continuous monitoring of decubitus ulcer of subjects lying on a bed. 13(1):5773. 1
- [23] Bo Li, Kaitao Xue, Bin Liu, and Yu-Kun Lai. Bbdm: Image-to-image translation with brownian bridge diffusion models. In *Proceedings of the IEEE/CVF Conference on Computer Vision and Pattern Recognition (CVPR)*, pages 1952–1961, 2023. 2, 3, 4, 5
- [24] Zhaoyu Li, Frances Lin, Lukman Thalib, and Wendy Chaboyer. Global prevalence and incidence of pressure injuries in hospitalised adult patients: A systematic review and meta-analysis. *International Journal of Nursing Studies*, 105:103546, 2020. 1
- [25] Jason J. Liu, Ming-Chun Huang, Wenyao Xu, and Majid Sarrafzadeh. Bodypart localization for pressure ulcer prevention. In *2014 36th Annual International Conference of the IEEE Engineering in Medicine and Biology Society*, pages 766–769, 2014. 2
- [26] Shuangjun Liu and Sarah Ostadabbas. Pressure eye: In-bed contact pressure estimation via contact-less imaging. *Medical Image Analysis*, 87:102835, 2023. 2
- [27] Shuangjun Liu, Xiaofei Huang, Nihang Fu, Cheng Li, Zhongnan Su, and Sarah Ostadabbas. Simultaneously-collected multimodal lying pose dataset: Enabling in-bed human pose monitoring. *IEEE Transactions on Pattern Analysis and Machine Intelligence*, 45(1):1106–1118, 2023. 2, 4, 5
- [28] Neevkumar Manavar, Hanno Gerd Meyer, Joachim Waßmuth, Barbara Hammer, and Axel Schneider. Attnfnet: feature aware depth-to-pressure translation with cgan training. *Frontiers in Medical Technology*, Volume 7 - 2025, 2025. 1, 2, 3, 4, 5, 6, 7, 8
- [29] Sam Mansfield, Katia Obraczka, and Shuvo Roy. Pressure injury prevention: A survey. *IEEE Reviews in Biomedical Engineering*, 13:352–368, 2020. 2
- [30] Lea Muller, Ahmed A. A. Osman, Siyu Tang, Chun-Hao P. Huang, and Michael J. Black. On self-contact and human pose. In *Proceedings of the IEEE/CVF Conference on Computer Vision and Pattern Recognition (CVPR)*, pages 9990–9999, 2021. 2
- [31] B. Osuagwu, E. McCaughey, and M. Purcell. A pressure monitoring approach for pressure ulcer prevention. *BMC Biomedical Engineering*, 5(1):8, 2023. 1, 2
- [32] Matthew J. Peterson, Wilhelm Schwab, Johannes H. Van Oostrom, Nikolaus Gravenstein, and Lawrence J. Caruso. Effects of turning on skin-bed interface pressures in healthy adults. *Journal of Advanced Nursing*, 66(7):1556–1564, 2010. 2
- [33] Matthew J Peterson, Nikolaus Gravenstein, Wilhelm K Schwab, Johannes H van Oostrom, and Lawrence J Caruso. Patient repositioning and pressure ulcer risk-monitoring interface pressures of at-risk patients. *Journal of Rehabilitation Research & Development*, 50(4), 2013. 2
- [34] Esteban J. Pino, Astrid Dörner De la Paz, Pablo Aqueveque, Javier A. P. Chávez, and Alejandra A. Morán. Contact pressure monitoring device for sleep studies. In *2013 35th Annual International Conference of the IEEE Engineering in Medicine and Biology Society (EMBC)*, pages 4160–4163, 2013. 1, 2
- [35] Devdip Sen, John McNeill, Yitzhak Mendelson, Raymond Dunn, and Kelli Hickie. A new vision for preventing pressure ulcers: Wearable wireless devices could help solve a common-and serious-problem. *IEEE Pulse*, 9(6):28–31, 2018. 1
- [36] Sumit Singh, Mohammad Hossein Anisi, Anish Jindal, and Delaram Jarchi. Smart multimodal in-bed pose estimation framework incorporating generative adversarial neural network. *IEEE Journal of Biomedical and Health Informatics*, 28(6):3379–3388, 2024. 2
- [37] Christian Szegedy, Vincent Vanhoucke, Sergey Ioffe, Jon Shlens, and Zbigniew Wojna. Rethinking the inception architecture for computer vision. In *Proceedings of the IEEE conference on computer vision and pattern recognition*, pages 2818–2826, 2016. 6
- [38] Thanh-Hai Tran, Duc Trung Nguyen, and Thanh Phuong Nguyen. Human posture classification from multiple viewpoints and application for fall detection. In *2020 IEEE Eighth International Conference on Communications and Electronics (ICCE)*, pages 262–267, 2021. 2
- [39] Ashish Vaswani, Noam Shazeer, Niki Parmar, Jakob Uszkoreit, Llion Jones, Aidan N Gomez, Łukasz Kaiser, and Illia Polosukhin. Attention is all you need. In *Advances in Neural Information Processing Systems*. Curran Associates, Inc., 2017. 3
- [40] Zhou Wang, A.C. Bovik, H.R. Sheikh, and E.P. Simoncelli. Image quality assessment: from error visibility to structural similarity. *IEEE Transactions on Image Processing*, 13(4): 600–612, 2004. 6
- [41] Yu Yin, Joseph P. Robinson, and Yun Fu. Multimodal in-bed pose and shape estimation under the blankets. In *Proceedings of the 30th ACM International Conference on Multimedia*, page 2411–2419, New York, NY, USA, 2022. Association for Computing Machinery. 2

- [42] Jiahui Yu, Xin Li, Jing Yu Koh, Han Zhang, Ruoming Pang, James Qin, Alexander Ku, Yuanzhong Xu, Jason Baldridge, and Yonghui Wu. Vector-quantized image modeling with improved VQGAN. In *International Conference on Learning Representations*, 2022. [2](#), [5](#)

Improving the Plausibility of Pressure Distributions Synthesized from Depth Image through Generative Modeling

Supplementary Material

7. Weight Optimization Loss

As shown in Sec. 3.2 total mass can be describes as Eq. (18)

$$m = \sum_{i=1}^N \frac{p_i A_i}{g} \quad (18)$$

where p_i is the pressure at i^{th} taxel with total N sensors, A_i is the area of the i^{th} taxel, and g is gravitational acceleration.

Assuming predicted pressure at i^{th} taxel is \hat{p} we can get Eq. (19), having area similar to actual taxel ($A_i = \hat{A}_i$).

$$\hat{m} = \sum_{i=1}^N \frac{\hat{p}_i \hat{A}_i}{g} \quad (19)$$

To optimize mass consistency, we define the loss as Eq. (20)

$$L_{WOL} = |m - \hat{m}| = \left| \sum_{i=1}^N \frac{p_i A_i}{g} - \sum_{i=1}^N \frac{\hat{p}_i \hat{A}_i}{g} \right| \quad (20)$$

Since $A_i = \hat{A}_i$ and $\sum_{i=1}^N A_i = A_{tot}$, we have Eq. (21):

$$\mathcal{L}_{WOL} = \frac{A_{tot}}{g} \left| \sum_{i=1}^N (p_i - \hat{p}_i) \right| \quad (21)$$

By the triangle inequality, we get Eq. (22).

$$\mathcal{L}_{WOL} \leq \frac{A_{tot}}{g} \sum_{i=1}^N |p_i - \hat{p}_i| \quad (22)$$

Therefore, reducing BM error is same as minimizing L_1 norm Eq. (23). It is more stable (Fig. 5) but it can't reduce mass plausibility when low frequency pressure ambiguity in actual distributions:

$$\mathcal{L}_{WOL2} = \sum_{i=1}^N |p_i - \hat{p}_i| = \|\mathbf{p} - \hat{\mathbf{p}}\|_1 \quad (23)$$

8. Effects of Data Normalization and Pre-processing

The choice of data normalization strategy significantly impacts the model's predictive performance for pressure distribution. Normalizing each pressure map individually is

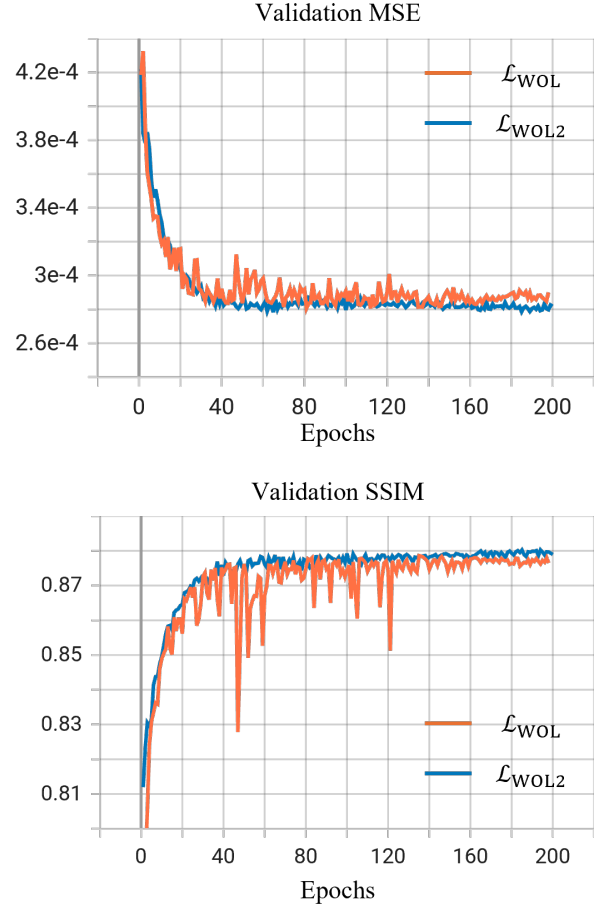


Figure 5. Comparison of validation MSE and SSIM performance between \mathcal{L}_{WOL} and \mathcal{L}_{WOL2} loss functions. Results are based on models trained for 200 epochs on 8 k real samples.

problematic, as pressure values are co-dependent on external factors like mattress softness. This approach can obscure the relationship between body mass and pressure features, leading to a decline in performance, as illustrated in Fig. 6. While prior work by Clever et al. [8] addressed this by normalizing pressure with body mass, their method required an separate network "Betanet" to predict body mass for denormalization. Betanet only infers BM and body-height and does not build any feature body parameter relationship.

Our approach employs a simpler global pressure normalization, where all pressure distributions are scaled into a $[0,$

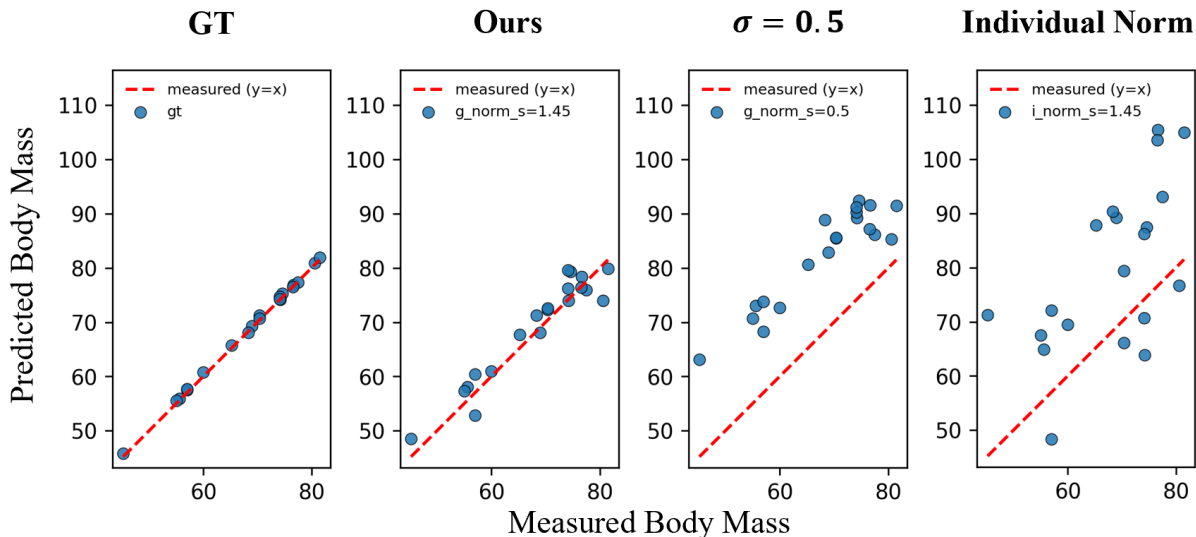


Figure 6. Comparison of BM estimation accuracy under different data normalization and pre-processing conditions. The scatter plot correlates predicted BM (derived from generated pressure distributions) with actual measurements (red dotted line). Blue points represent predictions from the proposed method trained on 8 k real samples. Notation: g_norm = global normalization; i_norm = individual normalization; σ = Gaussian filter standard deviation (e.g., $\sigma = 0.5$ denotes filtering with kernel width 0.5); GT denotes BM calculated from ground truth pressure distributions.

Table 9. Comparison of computational efficiency and model complexity. Metrics are reported for models trained on 8 k real samples over 100 epochs, with a batch size of 4.

Metric	Manavar et al. [28]	ours	BBDM	LBBDM
Batchsize	4			
Model	ATTNFNET-143M	ATTNFNET-11M	Openai U-Net	Openai U-Net
Pretrained Network	-	-	-	ATTNFNET-11M
Discriminator	PatchGAN	PatchGAN	-	PatchGAN
Input shape	(1, 54, 128)	(1, 54, 128)	(2, 256, 256)	(16, 32, 32)
Total Number of Parameters	143,635,940	11,761,018	59,303,489	258,114,312
Model Parameters Size (MB)	547.93	37.56	237.21	1032.46
FLOPs	3.92×10^{11}	6.71×10^9	1.98×10^{12}	1.29×10^{11}
training speed (it/s) per GPU	1.23	8.27	1.34	4.42
Training Speed (sec/epoch)	838	124	766	232.87
Memory Usage (GB/GPU)	17.2	2.2	21.3	6.5
validation speed (it/s) per GPU	4.99	102.34	4.1	52.50
validation time (sec/2700 img)	67.58	3.27	16643	1287.02
inference time (sec/img)	0.11	0.024	12.63	2.76
inference step	1	1	200	200

1] range based on a single maximum value from the entire dataset. This method proves to be both plausible and suitable for our approach (Fig. 6). However, a challenge arises from pre-processing steps like applying a Gaussian filter. While filtering smooths pressure distributions for better approximation, it can alter the pressure range differently across datasets by reducing low frequency high pressure spike to smoothen the values. For instance, extensive filtering on our real dataset reduces its pressure range to (0, 56)kPa, creating a mismatch with our synthetic data (0, 101)kPa. This discrepancy complicates the generation of valid samples when using WOL.

9. Model Parameters and Training Cost

The computational requirements for our models are summarized in Tab. 9. To improve training speed, we adopted the ATTNFNET architecture from Manavar et al. [28] but reduced its size. All models were trained for 100 epochs on a dataset of 8235 images with a batch size of 4. We utilized Distributed Data Parallel (DDP) on a single node equipped with two Tesla V100-PCI-E-32GB GPUs.

The proposed method achieves the fastest training and inference times while requiring the lowest total FLOPs. These efficiency gains demonstrate its capability and potential as a real-time monitoring system.

10. Model Configurations

This section provides the detailed hyperparameter settings and architectural configurations used in our experiments to facilitate reproducibility. Table 11 details the architecture of the AttnFNet generator and the openai U-Net denoising models (Pixel-space and Latent-space). Table 10 lists the training hyperparameters, including optimization settings and diffusion scheduling.

Figure 7 illustrates the proposed LBBDM training and inference pipeline for pressure synthesis. Fig. 7a shows the pretraining stage, where the ATTNFNET backbone is optimized using an image reconstruction loss as described in Sec. 3.3, together with architectural modifications such as the bottleneck modules *neck1*, *neck2* to reduce computational complexity, and no skip connection to remove feature influence from encoder to decoder. Fig. 7b depicts the latent-space denoising training strategy, and Fig. 7c outlines the inference procedure; fire symbols denote learnable layers and cold symbols indicate frozen layers.

We remove the sigmoid activation from the final layer of ATTNFNET+ILS in all experiments. Sigmoid produces bounded probability distributions that cause overestimation of both pressure values and body model BM parameters. Additionally, sigmoid saturation at extreme values compresses high/low pressure values into a narrow range, preventing the model from learning physically plausible pres-

sure distributions.

Table 10. Training Hyperparameters settings across experiments unless stated otherwise.

Hyperparameter	Value
<i>Optimization</i>	
Optimizer	Adam
Learning Rate	1×10^{-4}
Adam β_1	0.9
Batch Size	16
Max Epochs	200
<i>Diffusion Schedule</i>	
Diffusion Time Steps (T)	1000
Sampling Steps	200

Table 11. Network Architecture Configurations for the AttnFNet, as well as the U-Net architectures used for the Brownian Bridge Diffusion Model (BBDM) and Latent BBDM (LBBDM) variants.

Parameter	Value
<i>ATTNFNET</i>	
Input Resolution	54×128
Image size	256×256
Embedding Dim (C)	264
Encoding Depth	8
Attention Heads	12
Patch Size	16×16
Layers with global attention	(1, 2, 5, 8)
Encoder-decoder skip indices	(4, 6, 8)
<i>Diffusion Openai U-Net (BBDM / LBBDM)</i>	
Input Resolution	$256 \times 256 / 32 \times 32$
Base channel width	64 (Pixel) / 128 (Latent)
Channel Multipliers	(1, 4, 8)
Attention Resolutions	(32, 16, 8) / (32, 16, 4)
Num Res Blocks	2
Attention Heads	64
Conditioning	concat
<i>Discriminator</i>	
Cond/ Uncond discriminator	PatchGAN
Features per layer	(64, 128, 256, 512)
patch size	62×62

11. Realtime Monitoring

To preliminarily evaluate real-time capability, we conducted a temporal analysis comparing two versions of our method:

one trained on 8 k real samples and another on a larger 203 k mixed dataset. A qualitative visual comparison is presented in Fig. 8.

Our findings show evidence of no overfitting and highlight the need for a diverse training dataset. As shown in Fig. 8, the model trained on 203 k samples demonstrates superior robustness. When the bed is empty, it generates low-amplitude noise. In contrast, the model trained on only 8 k samples is prone to hallucination, inferring human-like pressure patterns where none exist.

We identified several limitations in the current real-time partial evaluation. First, while Fig. 8 demonstrates real-time capabilities, the current API (Application Programming Interface) version is not optimized for speed. The current method does not explicitly enforce temporal consistency, which could lead to fluctuations between consecutive frames. A thorough zero-shot quantitative evaluation on unseen environments is needed. Addressing these aspects constitutes a clear direction for future work.

12. LBBDM Synthetic Pre-Training Results

This section presents results for a special case of LBBDM pre-training. Figure 7 illustrates the training strategy of the conditional LBBDM model as a schematic diagram. In contrast to the method described in Sec. 3.3, we tested the capability of conditional LBBDM to generate real samples when the ATTNFNET model with ILS was pre-trained on synthetic data, while post-training and testing were performed exclusively on real samples.

Pre-training with synthetic data leads to an increase in MSE, as shown in Tab. 12. These results indicate the importance of real samples during pre-training. A visual comparison of both cases is presented in Fig. 11.

Table 12. Test set MSE in kPa^2 for uncovered (Ucov), covered at 1 mm, covered at 3 mm, and overall poses. The results compare LBBDM pre-trained on real samples (LBBDM 8 k) versus synthetic-only pre-training (LBBDM-synth).

Method	Ucov	cov (1mm)	cov (3mm)	overall
LBBDM 8 k	0.9047	1.0590	1.0803	1.0149
LBBDM-synth	1.0463	1.2318	1.2514	1.1765

13. Additional Results

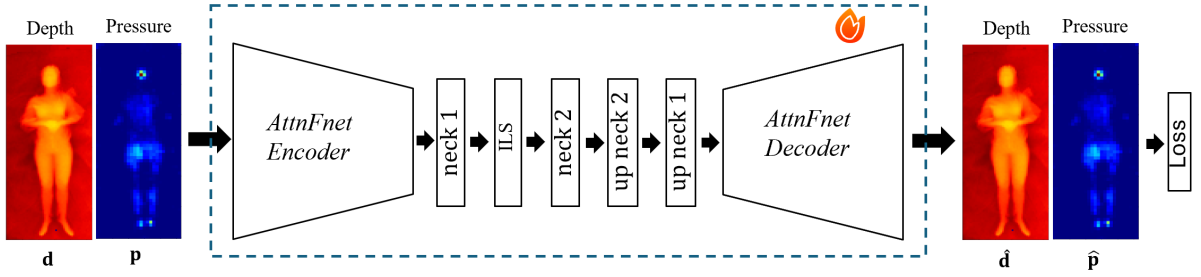
Figure 9 illustrates the individual and combined impact of ILS and WOL on BM plausibility. The use of ILS enhances BM consistency, whereas WOL ensures the generated distribution aligns closely with the participant’s ideal BM. Integrating both components results in improved consistency and significantly reduced BM estimation error.

Figure 10 demonstrates BM adaption capability of ILS via anthropometric conditioning. Using a fixed depth input, the model synthesized three distinct pressure distributions: $\hat{\mathbf{p}}$ using actual parameters ($m = 45.2$, $h = 1.51$, $g = \text{Female}$), $\hat{\mathbf{p}}_2$ with reduced mass ($m = 5.2$, $h = 1.51$, $g = \text{Female}$), and $\hat{\mathbf{p}}_3$ with increased mass ($m = 145.2$, $h = 1.51$, $g = \text{Female}$). Reducing the input mass decreases the overall inferred pressure, while increasing it amplifies pressure, particularly in the pelvic region where high loads are expected. This adaptability suggests the system can accommodate patient weight fluctuations in real-world deployments by adjusting conditioning inputs, without other adjustments to the model.

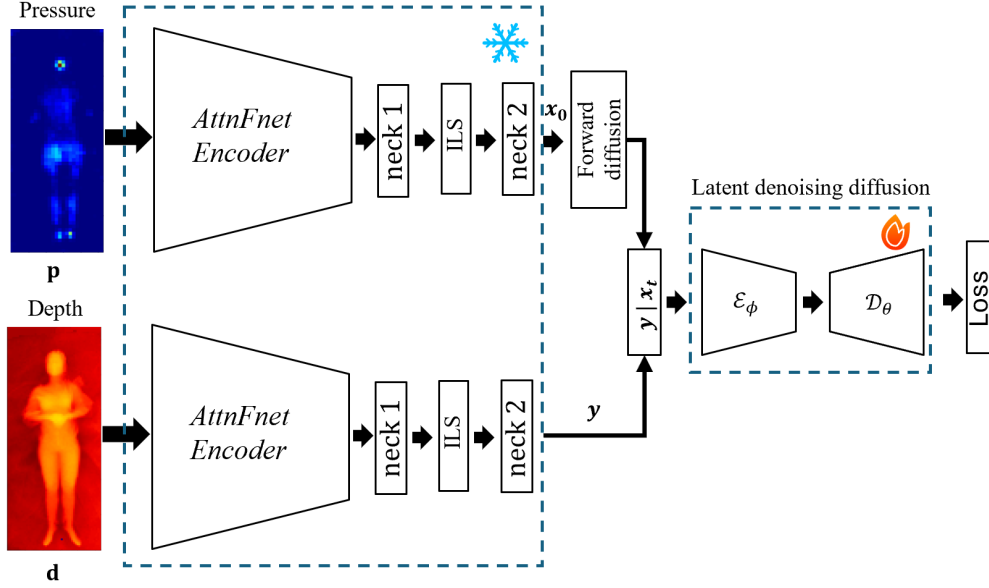
The derived BM values are plotted in Fig. 10. While the BM calculated from $\hat{\mathbf{p}}_2$ and $\hat{\mathbf{p}}_3$ follows the trend of the conditioning inputs, it does not perfectly match the target values. This discrepancy arises because the input depth profile remains static, reflecting the subject’s original profile—which conflicts with the synthetic mass prompts. Conversely, the model depth - anthropometric relationship remains intact when using actual parameters $\hat{\mathbf{p}}$. Future work can lead to validating this method against ground-truth data from controlled weight gain and loss scenarios.

Qualitative results are shown in Fig. 11, including comparisons with LBBDM with a pretrained VQGAN and LBBDM with pretraining on synthetic data. Complex scenarios, such as resting poses covered by a blanket, challenge all evaluated models. In these cases, baselines like BBDM and BPWnet often hallucinate incorrect postures. In contrast, the proposed method reduces error by blurring unseen regions rather than generating misleading features.

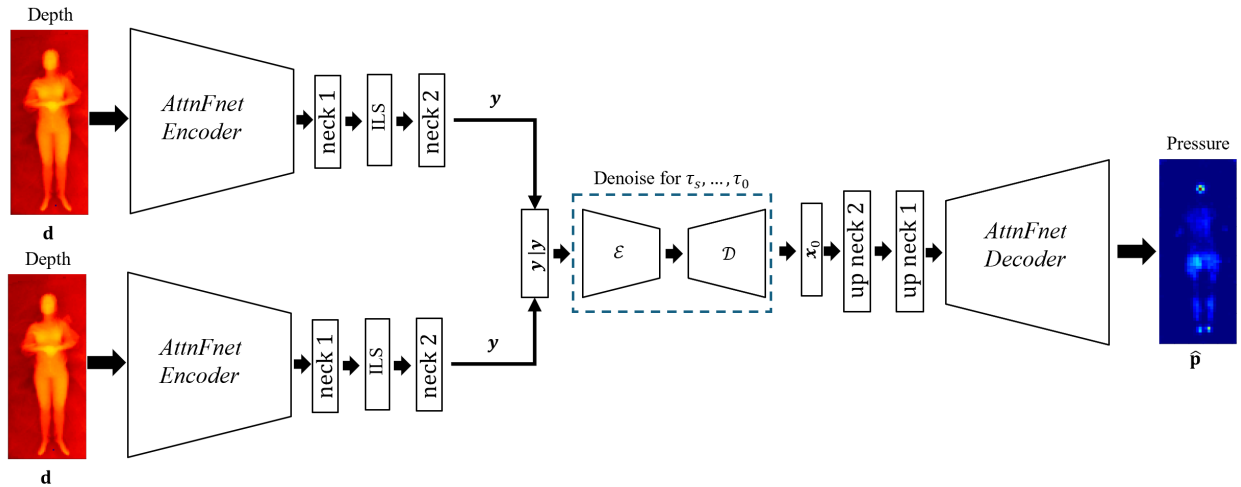
Figure 12 quantifies the MAE across supine, left-side, and right-side postures under three conditions. Consistent with expectations, the pelvic region exhibits the largest errors across all methods. Uncovered postures yield the lowest deviations, while scenarios involving a 3mm blanket result in the highest deviations due to occlusion. The proposed method and BBDM + ILS leads to lower MAE in the pelvic region.



(a) pretraining of the ATTNFNET model with image reconstruction objective.



(b) training strategy of the denoising model in latent space



(c) schematic diagram of the inference.

Figure 7. schematic of proposed LBBDM training strategy and inference.

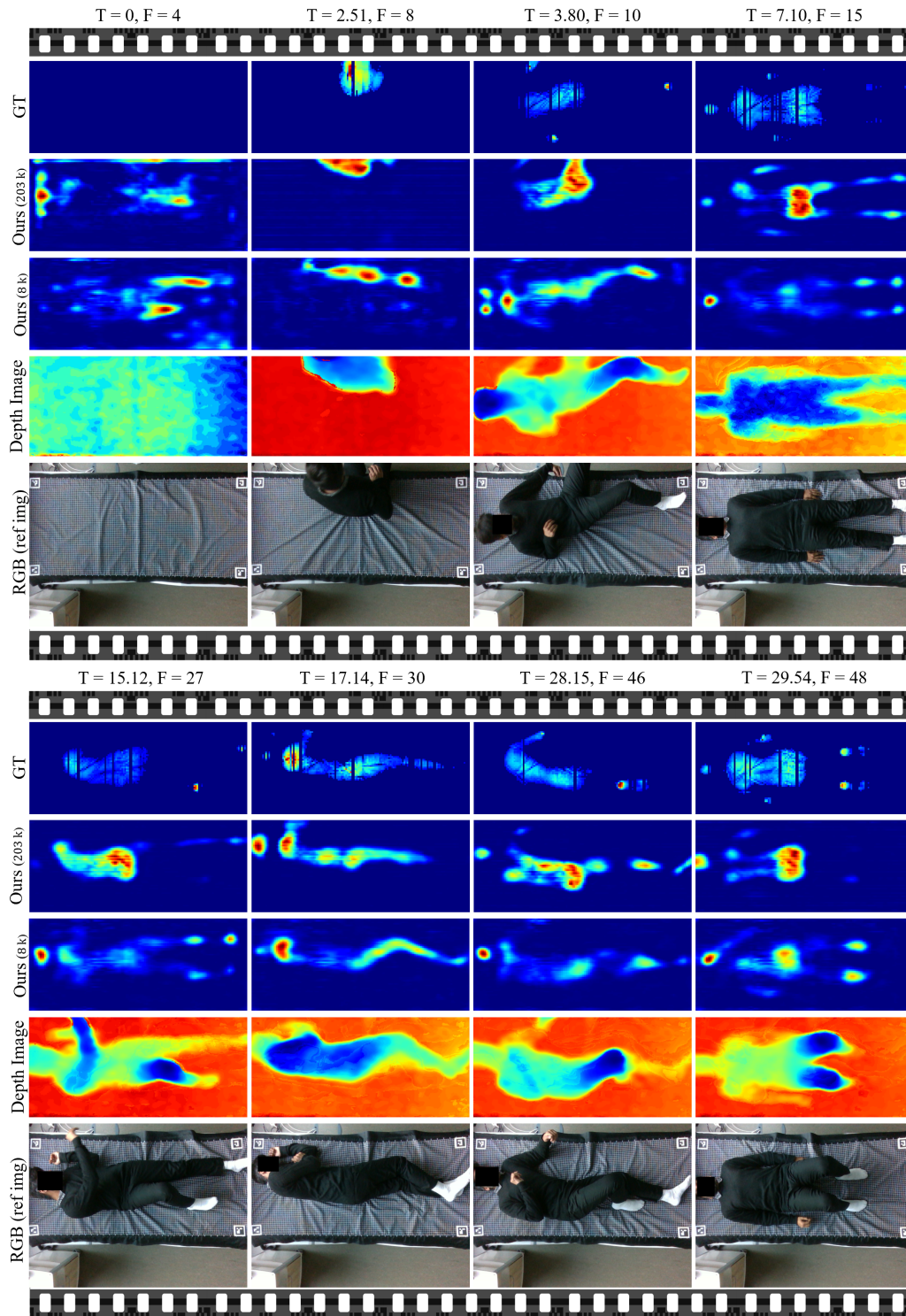


Figure 8. Qualitative evaluation of real-time pressure prediction. We compare the ground truth (GT) pressure distribution against predictions from models trained on 203 k (Ours 203 k) versus 8 k (Ours 8 k) samples. Corresponding depth inputs and RGB reference images are shown for context. Timestamps (T) and frame numbers (F) indicate the temporal progression of the trial.

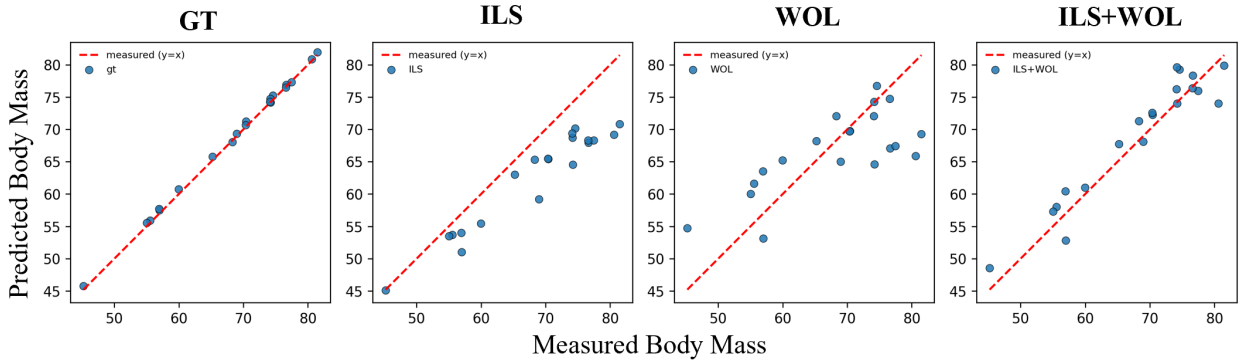


Figure 9. Impact of proposed components on BM estimation consistency. The scatter plot compares predicted BM ($\hat{B}M$) against measured BM (red dotted line) and ground truth (GT) values (blue dots align with red dotted line) under different training configurations (blue points). **ILS**: Informed Latent Space only; **WOL**: Weight Optimization Loss only; **ILS+WOL**: Combined approach. All models were trained on 8 k real samples.

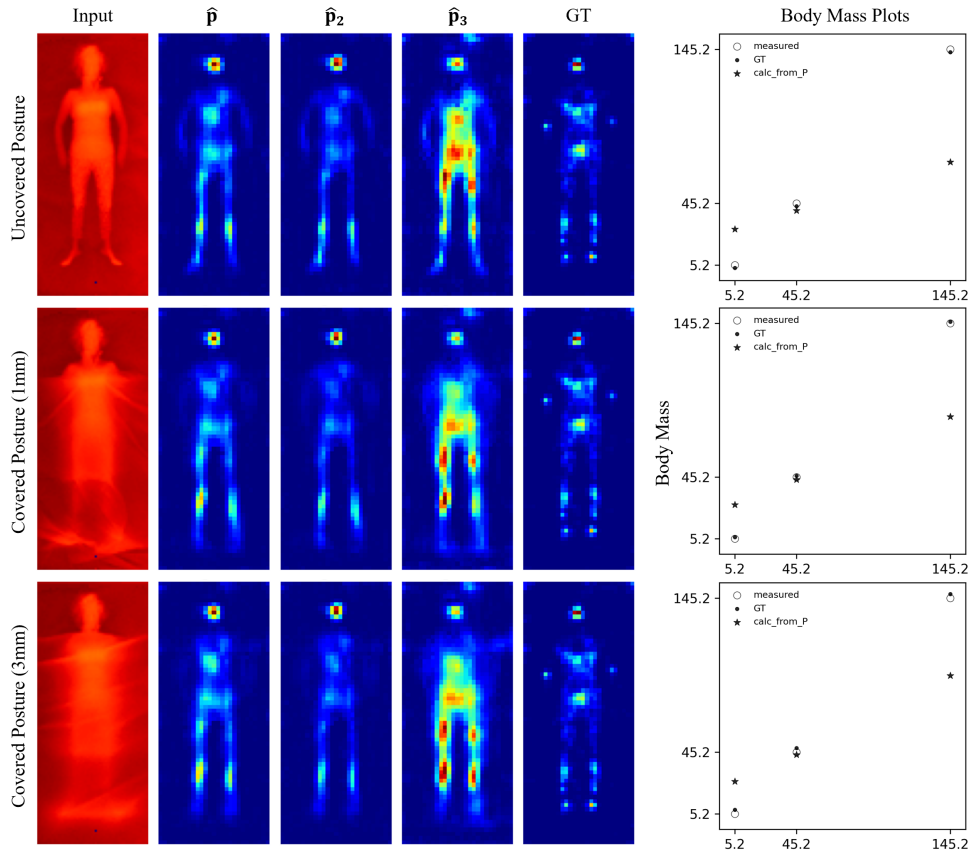


Figure 10. Visualization of diverse pressure distributions generated from a single depth input using different anthropometric prompts. **Left**: Predicted pressure maps \hat{p} , \hat{p}_2 , and \hat{p}_3 correspond to varying mass inputs ($m = 45.2, 5.2,$ and 145.2 kg, respectively) while holding height ($h = 1.51$ m) and gender ($g = \text{Female}$) constant. **Right**: Corresponding computed Body Mass (BM) plots. Models were trained on 203 k mixed (real + synthetic) samples.

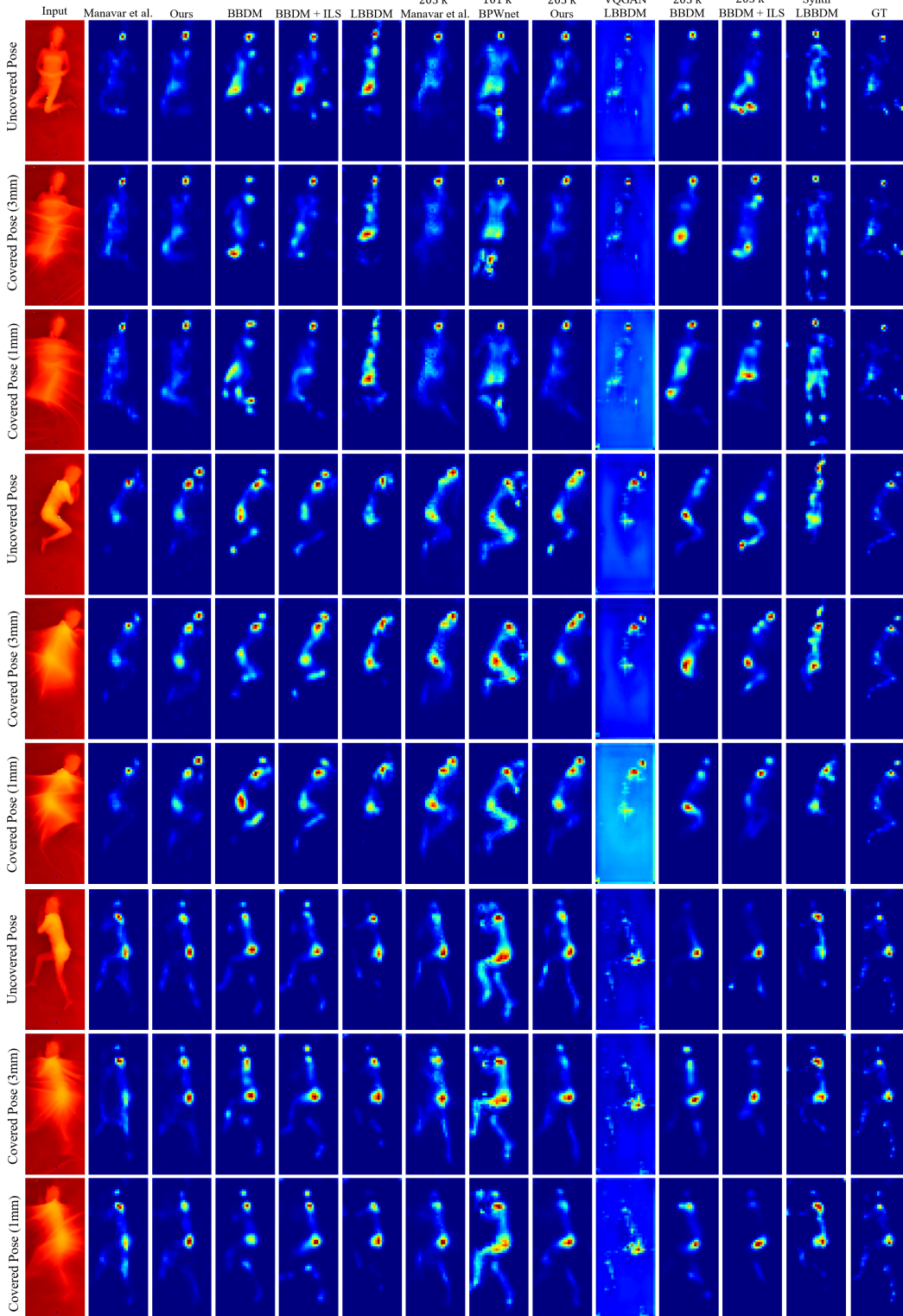


Figure 11. Qualitative comparison of predicted pressure distributions across different methods. Rows represent distinct test samples, while columns display the outputs from competing models against the ground truth (GT). VQGAN represents pretraining happened with the VQGAN model on the CelebHQ dataset, synth represents ATTNFNET-11M pretrained on synthetic data and post training performed on real data.

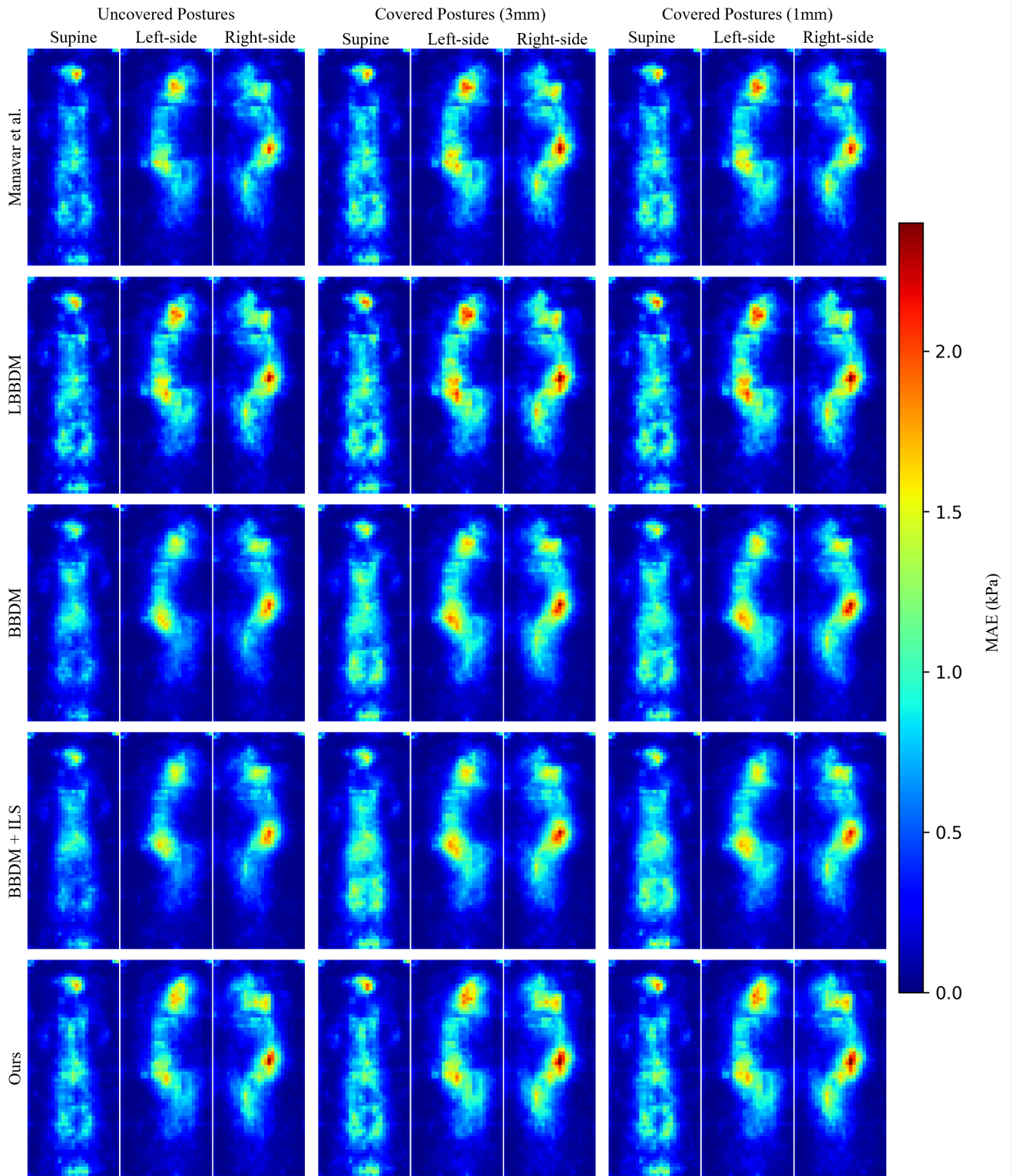


Figure 12. Analysis of MAE posture deviations across supine, left-side, and right-side positions. Rows correspond to different training methods, while columns represent varying cover conditions (e.g., no cover vs. blanket). All models were trained on 8 k real samples.